

## A 650 km<sup>2</sup> Miocene strewnfield of splash-form impact glasses in the Atacama Desert, Chile

Gattacceca J. <sup>1,\*</sup>, Devouard B. <sup>1</sup>, Barrat Jean-Alix <sup>2</sup>, Rochette P. <sup>1</sup>, Balestrieri M.L. <sup>3</sup>, Bigazzi G. <sup>3</sup>, Ménard G. <sup>1</sup>, Moustard F. <sup>1</sup>, Dos Santos E. <sup>4</sup>, Scorzelli R. <sup>5</sup>, Valenzuela M. <sup>6,7</sup>, Gounelle M. <sup>8</sup>, Debaille V. <sup>9</sup>, Beck P. <sup>10</sup>, Bonal L. <sup>10</sup>, Reynard B. <sup>11</sup>, Warner M. <sup>12</sup>

<sup>1</sup> CNRS, Aix Marseille Univ, IRD, INRAE, CEREGE, 13545 Aix-en-Provence, France

<sup>2</sup> Univ Brest, CNRS, IRD, Ifremer, LEMAR, F-29280 Plouzané, France

<sup>3</sup> CNR, Institute of Geosciences and Earth Resources, 56124 Pisa, Italy

<sup>4</sup> Instituto de Ciência e Tecnologia, Universidade Federal dos Vales do Jequitinhonha e Mucuri UFVJM, Diamantina, MG 39100-000, Brazil

<sup>5</sup> Centro Brasileiro de Pesquisas Físicas – CBPF, Rio de Janeiro, RJ 22290-180, Brazil

<sup>6</sup> Departamento de Ciencias Geológicas, Universidad Católica del Norte, Av. Angamos 0610, Antofagasta, Chile

<sup>7</sup> Millennium Institute of Astrophysics, Av. Vicuña Mackenna, 4860, Macul, Santiago, Chile

<sup>8</sup> Muséum national d'Histoire naturelle, Sorbonne Universités, CNRS, IMPMC, 75005 Paris, France

<sup>9</sup> Laboratoire G-Time, Université Libre de Bruxelles, 1050 Brussels, Belgium

<sup>10</sup> Univ. Grenoble Alpes, CNRS, IPAG, 38400 Grenoble, France

<sup>11</sup> Univ Lyon, ENSL, UCBL, CNRS, LGL-TPE, 69342 Lyon, France

<sup>12</sup> NSF National Optical-Infrared Astronomy Research Laboratory, Avda Juan Cisternas 1500, La Serena, Chile

\* Corresponding author : J. Gattacceca, email address : [gattacceca@cerege.fr](mailto:gattacceca@cerege.fr)

### Abstract :

Glassy ejecta are associated to a limited number of impact craters, and yet hold key information about hypervelocity impact processes. Here we report on the discovery of a ~650 km<sup>2</sup> impact glass strewnfield in the Central Depression of the Atacama Desert. These cm-sized splash-form objects, that we refer to as atacamaites, are essentially composed of a dacitic glass formed by high-temperature melting of local magmatic rocks, with the addition of a variable iron meteorite contamination, 5 wt.% on average. The most likely nature for the impactor is the IIAB iron group. The fission-track plateau method, on two samples, yielded a mean formation age of Ma. No associated impact crater has been discovered so far, suggesting it may be a relatively small, km-sized crater. The glassy nature, aerodynamic shapes, elevated formation temperature, and low water content are reminiscent of tektites. However, their small size, heterogeneity, oxidation state, significant contamination by the impactor, and likely more proximal provenance distinguish them from tektites. Atacamaites have no equivalent among the few known terrestrial ejected impact glasses, and increase the intriguing diversity of such products that we propose to name “tektoids”.

---

## Highlights

► Discovery of a ~650 km<sup>2</sup> impact glass strewnfield in the Central Depression of the Atacama Desert. ► cm-sized splash-form glassy objects, called atacamaites, formed by impact at  $7.8 \pm 0.26$  Ma. ► Dacitic composition with the addition of a variable iron meteorite contamination, 5 wt.% on average. ► Small size, heterogeneity, oxidation state, contamination level distinguish them from tektites. ► Impactor was an iron meteoroid, very likely from the IIAB group.

**Keywords** : impact glasses, Atacama Desert, tektites

## 38 **1. Introduction**

39 Natural silicate glasses generated by hypervelocity impact encompass melts in breccia, and  
40 impact glasses *per se*, i.e., individual pieces of glasses with minor proportions of relict  
41 unmolten grains or quenched crystals (Dressler and Reimold, 2001; Glass and Simonson, 2013;  
42 Koeberl, 2014). Tektites are nearly pure impact glasses ballistically ejected at long distance  
43 from their source, and bear typical splash-form shapes. Presently, five tektite strewnfields are  
44 recognized (Table 1). Beside tektites, more proximal splash-form impact glasses are found  
45 associated with a small number of craters (Table 1). The formation of tektites and other ejected

46 impact glasses remains largely enigmatic, partly due to their small number of occurrences and  
47 variable characteristics. Here we report on the discovery of impact glasses from the Atacama  
48 Desert (referred to as “atacamaites”).

49

## 50 **2. Geological setting, strewnfield, macroscopic description**

51 The atacamaite strewnfield is located in the Central Depression of the Atacama Desert between  
52 the Coastal Cordillera to the west and the Precordillera (Cordillera Domeyko) to the east. Local  
53 rocks are Middle Jurassic to Lower Eocene calc-alkaline volcanic and intrusive rocks present  
54 as rocky reliefs and smooth landforms, partly covered unconformably by a thin layer of Upper  
55 Miocene-Pliocene alluvial deposits consisting in unconsolidated polymict gravels supported  
56 by a sandy matrix deposited between 10 Ma and 1 Ma (Espinoza et al., 2012).

57 Centimeter-sized dark glassy stones were first noticed in 2011 by one us (MW). Subsequent  
58 dedicated field work allowed collecting ~23,000 samples<sup>1</sup> from over 100 discrete locations  
59 over a surface of ~650 km<sup>2</sup> (Fig. 1). The borders of the strewnfield are constrained by sites  
60 where a 60 man.minutes search did not reveal a single atacamaite. A few tens of similar-looking  
61 glass samples have been found sporadically about 40 km northwest of the strewnfield. The  
62 maximum dimension of the strewnfield is therefore at least 100 km. Samples were encountered  
63 lying on the desert surface, and more abundant, up to several tens per m<sup>2</sup>, in gravels  
64 concentrations. They were encountered on all geological units present in the area. They range  
65 from 1 to 35 mm in length, with an average mass of  $0.55 \pm 0.48$  g ( $1\sigma$ ), and a maximum mass  
66 of 5.9 g. They are pieces of black glass, with minor vesicularity. The vast majority of samples  
67 display globular forms, with rare button, dumbbell, or teardrop shapes (Fig. 2A). The average  
68 shape parameters L (longest over intermediate axes) and F (intermediate over short axes) are

---

<sup>1</sup> Research material is available upon request to the first author

69 1.74±0.57 and 1.43±0.30 (n=989). Most pieces show a somewhat dull abraded surface  
70 attributed to transport and/or sand blasting. A limited number of samples show a shiny surface  
71 with small droplets stuck to the surface, as well as contorted splash-forms.

72

### 73 **3. Methods**

74 Optical microscopy was performed with a Leica DM2500P petrographic microscope at  
75 CEREGE, France. Backscattered electron (BSE) images, microanalyses by energy dispersive  
76 spectroscopy (EDS) and chemical maps were acquired with a Hitachi S3000-N Scanning  
77 Electron Microscope (SEM) operated at 15 kV and equipped with a Bruker X-ray XFlash  
78 detector and a Spirit analyzer at CEREGE. Semi-quantitative analyses used a variety of natural  
79 and synthetic standards.

80 The grain density was measured with a Quantachrome helium stereopycnometer at  
81 CEREGE. Magnetic susceptibility was measured with an Agico MFK1 susceptibility at  
82 CEREGE.

83 Whole-rock major, trace elements and isotopic compositions were determined at the  
84 PSO/IUEM (Pôle Spectrométrie Océan, Institut Universitaire Européen de la Mer, Brest,  
85 France). 100-150 mg of atacamaïtes were digested on a hot plate heated to 125°C, using  
86 sequential mixtures of HF/HNO<sub>3</sub>, HNO<sub>3</sub> and HCl. The aliquots of the obtained solutions were  
87 used for the determination of major and trace element concentrations, Sr and Nd isotopic  
88 compositions. Major elements, Ni and Co abundances were analyzed by inductively coupled  
89 plasma-atomic emission spectrometry (ICP-AES) using a Horiba Jobin Yvon Ultima  
90 spectrometer and following the analytical procedure of Cotten et al. (1995). Relative standard  
91 deviations are < 2%. The accuracy is better than 7% for Na and P, and much better than 3%  
92 for the other elements. Trace element concentrations were measured with a Thermo® Element2  
93 ICP-SFMS (inductively coupled plasma-sector field mass spectrometer). Concentrations were  
94 determined following the procedure described by Barrat et al. (2012, 2016). **Based on results**  
95 **obtained on many standards, the reproducibility and accuracy are always better than 5%.**  
96 Strontium and Nd fractions were prepared following conventional ion exchange techniques.  
97 They were analyzed using a Thermo® Triton TIMS (thermal ionization mass spectrometer).  
98 Isotopic ratios were normalized against <sup>86</sup>Sr/<sup>88</sup>Sr = 0.1194 and <sup>146</sup>Nd/<sup>144</sup>Nd=0.7219. The values

99 obtained for NBS 987 and La Jolla standards during the course of the study are respectively  
100  $^{87}\text{Sr}/^{86}\text{Sr} = 0.710254 \pm 0.000003$  ( $2 \sigma$ ,  $n=8$ ) and  $^{143}\text{Nd}/^{144}\text{Nd} = 0.511830 \pm 0.000003$  ( $2 \sigma$ ,  $n=6$ ).

101 Quantitative major element analyses were conducted using electron microprobe analyses  
102 (EPMA) Cameca SX100 at UPMC CAMPARIS facility. The operating conditions were 15 kV  
103 accelerating voltage with a current of 10 nA and a counting time of 30 s, with a focused beam  
104 ( $1 \mu\text{m}$ ). Both natural and synthetic standards were used for calibration: albite for Na; anorthite  
105 for Al; apatite for P; diopside for Mg, Si, Ca; orthoclase for K;  $\text{MnTiO}_3$  for Mn and Ti;  $\text{Fe}_2\text{O}_3$   
106 for Fe; and NiO for Ni. Typical detection limits are (in ppm): 450 for Na, 470 for Al, 710 for  
107 Mg, 670 for Si, 610 for Ca, 600 for K, 1040 for Mn, 420 for Ti, 1270 for Fe, and 1330 for Ni.

108  $^{57}\text{Fe}$  Mössbauer spectroscopy ( $^{57}\text{Fe}$ -MS) was conducted at CBPF, Brazil. It was performed  
109 at room temperature (RT) in standard transmission geometry using a 25 mCi  $^{57}\text{Co}/\text{Rh}$   
110 radioactive source in sinusoidal mode. Spectra were recorded for 96 hours in a 512 channels  
111 spectrometer and the drive velocity calibration was taken at room temperature (RT) with an  $\alpha$ -  
112 Fe foil. All isomer shifts reported in this work are given relative to  $\alpha$ -Fe at RT. The error in  
113 source velocity is less than 1%. For each studied sample, about 100 mg of material was grinded  
114 and used as Mössbauer absorber. Spectral analysis was performed with the two-dimensional  
115 extended Voigt-based fitting method (x-VBF) developed by Lagarec and Rancourt (1997). This  
116 method provides the total Probability Density Distribution (PDD) of static hyperfine  
117 parameters allowing the analysis of independent, partially or fully correlated arbitrary-shape  
118 partial distributions of isomer shift ( $\delta$ ), quadrupole splitting ( $\Delta$ ) and, for magnetically ordered  
119 materials, hyperfine magnetic Zeeman splitting ( $z$ ).

120 Micro-infrared spectroscopy was performed using a Bruker Hyperion Microscope coupled  
121 with a Vertex 70 FTIR (Fourier-transform infrared spectroscopy) spectrometer at the Institut  
122 de Planétologie et d'Astrophysique de Grenoble, France. Double polished sections of atacamite  
123 were prepared with thicknesses in the 300-600  $\mu\text{m}$  range. Transmission spectra were obtained  
124 using 32 scans at a spectral resolution of 4  $\text{cm}^{-1}$  for areas of typical size 100  $\mu\text{m}$  x 100  $\mu\text{m}$ . The  
125 absorbance due to  $\text{H}_2\text{O}$  in the glasses was measured at 3570  $\text{cm}^{-1}$  and the water contents were  
126 estimated using a Molar Absorptivity of 74.8  $\text{L}/(\text{mol}\cdot\text{cm})$  (Beran and Koeberl, 1997) and a  
127 density of 2430  $\text{kg}/\text{m}^3$  (as measured by helium pycnometry, see below).

128 Raman spectra of  $\text{SiO}_2$  rich inclusions were obtained at Laboratoire de Géologie de Lyon  
129 (ENS Lyon, France) using a LabRAM HR800 Evolution spectrometer with a confocal Czerny-  
130 Turner geometry and a laser source of 532 nm in wavelength. Spectra were acquired using a

131 laser power of 10 mW, and 25 accumulations of 5 to 15s. Gratings with 600 groove/mm were  
132 used to cover the frequency range 60 to 1300 cm<sup>-1</sup>.

133 Fission-tracks ages were obtained following the protocol established at the Institute of  
134 Geosciences and Earth Resources (IGG-CNR) of Pisa (Laurenzi et al., 2007): samples JG26  
135 and PT7E were handmade crushed to reduced them in multiple pieces. A fraction of each  
136 sample was irradiated in the Lazy Susan (Cd ratio 6.5 for Au and 48 for Co) facility of the  
137 Triga Mark II reactor of LENA, University of Pavia (Italy). After irradiation, fractions for  
138 spontaneous and induced track counting were mounted in epoxy resin, polished, and etched for  
139 track revelation (120s in 20% HF at 40°C). Tracks were counted under a Jena-Jenaval  
140 microscope with a magnification of 500x. Track-diameters in glass were measured with a  
141 magnification of 1000x with a digital tablet. We corrected the obtained ages for track annealing  
142 (i.e., track shortening) that occurs even at ambient temperature, and that is revealed by a  
143 spontaneous to induced track-diameter ratio  $D_s/D_I < 1$  (Storzer and Wagner, 1969).  
144 Spontaneous track sizes are reduced by ~ 30 % in JG26 and ~ 20 % in PT7E (Table 4). The  
145 correction follows the plateau method which consists in re-establishing, through laboratory  
146 thermal treatments, identical etching efficiencies for spontaneous and induced tracks (Storzer  
147 and Poupeau, 1973). In this study, following the common practice, only one heating step (4h  
148 at 220°C) was used (e.g., Sandhu et al., 1993).

149

### 150 **3. Petrography**

151 Atacamaites are entirely glassy in the vast majority of cases. They contain a variable proportion  
152 (few vol.%) of vesicles ca. 100 µm in diameter. Complex schlieren textures are observed  
153 (Figure 2B). Some samples have texture suggesting formation by accretion of molten beads of  
154 a few hundreds µm in size (Fig. 2a, Fig. 2c). Lechatelierite (nearly pure silica glass), identified  
155 in particular by Raman spectroscopy (Fig. S1), is present as small patches with size ranging  
156 from a few µm to more than 2 mm. Some have a whirling texture indicating strong deformation  
157 in liquid state (Fig. 2D).

158 In the most magnetic samples, iron oxides can be observed as dendritic assemblages of  
159 micrometer-sized crystallites forming threads or globules (Fig. 2E). These iron oxides were  
160 observed only in samples with magnetic susceptibility higher than  $\sim 350 \times 10^{-9} \text{ m}^3/\text{kg}$ , which  
161 make up 10% of our collection. A few relict grains of incompletely molten quartz were  
162 observed in rare samples that were selected among several hundreds because of their abnormal,  
163 highly vesicular aspect.

164 The grain density, measured by helium pycnometry on three separate atacamaite batches  
165 totaling 67 g, is  $2.48 \text{ g}/\text{cm}^3$ . The water content estimated by micro infrared spectroscopy is  
166  $177 \pm 32 \text{ ppm}$  (19 analyses, on 4 samples).

167

#### 168 **4. Geochemistry**

169 Magnetic susceptibility of atacamaites shows a log normal distribution with a median of 169  
170  $10^{-9} \text{ m}^3/\text{kg}$  compatible with a paramagnetic behavior, i.e., iron diluted in the glass (Rochette et  
171 al., 2015). Magnetic susceptibility correlates roughly with the bulk Ni content, indicating that  
172 it may be a good proxy to select samples with higher extraterrestrial contamination (Rochette  
173 et al., 2015). Therefore, in addition to regular samples, we selected specifically samples with  
174 high susceptibility (above  $300 \times 10^{-9} \text{ m}^3/\text{kg}$ , and up to  $3593 \times 10^{-9} \text{ m}^3/\text{kg}$ ) for bulk major and  
175 trace elements analyses, and EPMA.

176 Average bulk chemical composition of atacamaites (Table 2) is similar to a K-rich dacite, with  
177  $\text{SiO}_2 = 64.1 \text{ wt.}\%$ ,  $\text{Na}_2\text{O} + \text{K}_2\text{O} = 6.54 \text{ wt.}\%$ , and  $\text{K}_2\text{O} = 2.98 \text{ wt.}\%$  ( $n=15$ ). Iron is extremely  
178 heterogeneous ( $\text{FeO}_{\text{total}}$  ranges from 4.58 to 14.2 wt.%), and correlates with Ni and Co  
179 abundances that are high, up to 4800 ppm and 400 ppm, respectively (Fig. 3). At microscopic  
180 scale, EPMA (Table S1) show that the Fe-rich regions are also enriched in Ni, with a good  
181 correlation between Ni and Fe contents (Fig. 3a).



182 Chondrite-normalized REE patterns are similar for all samples, characterized by a  $\text{La}_N/\text{Lu}_N$   
183 ratio ranging from 7.47 to 8.00 and a significant negative Eu anomaly ( $\text{Eu}/\text{Eu}^*=0.50$ ),  
184 compatible with a dacitic target (Fig. 4). Strontium and Nd isotopic compositions, measured  
185 for five samples, also reveal fairly homogeneous isotopic compositions, with  $^{87}\text{Sr}/^{86}\text{Sr} = 0.7076$   
186  $\pm 0.0001$  and  $^{143}\text{Nd}/^{144}\text{Nd} = 0.512636 \pm 0.000006$  (Fig. 5).

187

## 188 **5. Mössbauer spectroscopy**

189 Five atacamaite samples were studied for Mössbauer spectroscopy. The room temperature  $^{57}\text{Fe}$   
190 Mössbauer spectra of all samples were fitted with two components described as distribution 1  
191 (D1) and distribution 2 (D2). A typical spectrum is shown in Figure 6a. Only sample J338-23,  
192 selected for its high magnetic susceptibility, exhibited a magnetic phase ordered at room  
193 temperature, identified as magnetite and fitted with two sextets assigned as Fe-A and Fe-B.  
194 The former, with average hyperfine field ( $B_{\text{hf}}$ )  $\sim 49$  T, corresponds to  $\text{Fe}^{3+}$  at tetrahedral sites  
195 in magnetite while the latter ( $B_{\text{hf}} \sim 45$  T) to  $\text{Fe}^{2.5+}$  at octahedral sites (Cornell and Schwertmann  
196 2003).

197 Despite the differences in relative areas, all samples exhibit similar average hyperfine  
198 parameters for D1 and D2 (Table 3). The main distribution D1 presents average isomer shift  
199  $\langle\delta\rangle \sim 0.88 - 1.02$  mm/s and average quadrupole splitting  $\langle\Delta\rangle \sim 1.95 - 2.19$  mm/s that is  
200 usually associated to  $\text{Fe}^{2+}$  in octahedral coordination, as shown in previous works on tektites  
201 and other natural glasses (Dunlap and Sibley 2004; Stewart et al. 2003). However, as pointed  
202 out by Rossano et al. (1999), D1 could also be assigned to a five-fold co-ordinated  $\text{Fe}^{2+}$ . In  
203 contrast, distribution D2 with  $\langle\delta\rangle \sim 0.49 - 0.56$  mm/s and  $\langle\Delta\rangle \sim 0.76 - 0.83$  mm/s is more  
204 likely to be  $\text{Fe}^{3+}$  in octahedral coordination (Johnson and Johnson 2005). Although previous  
205 works on tektites (e.g., Australasian) indicate  $\langle\Delta\rangle \sim 0.00$  mm/s for  $\text{Fe}^{3+}$  (Dunlap and Sibley

206 2004), some impact glasses (e.g., Aouelloul glass, irghizites) show iron species with  
207 appreciable quadrupole splitting that is very much  $\text{Fe}^{3+}$ -like (Dunlap and McGraw 2007). In  
208 this sense, the Mössbauer data of atacamaites have much more in common with these impact  
209 glasses. Indeed, except for the presence of magnetite in sample J338-23, the shape of all  
210 Mössbauer spectra is very similar to the one of Irghizite impact glass (see Fig. 1c, in Dunlap  
211 and McGraw 2007).

212 As shown in Fig. 6b and 6c, the isomer shift and quadrupole splitting for D1 and D2 are  
213 distributed around their average values, in accordance with the wide range of local distortion  
214 of cation environments observed in glasses. As a result, D1 and D2 may contain small  
215 contributions due to tetrahedrally coordinated iron ( $\text{Fe}^{2+}$  or  $\text{Fe}^{3+}$ ), as already identified in  
216 silicate glasses (Johnson and Johnson 2005; Stewart et al. 2003). In addition, although the  
217 occurrence of electron delocalization has not been reported for previously studied tektites  
218 (Rossano et al. 1999), this effect cannot be neglected in our samples - electron delocalization  
219 results in average value of isomer shift (0.5 – 0.9 mm/s) that can be assigned to  $\text{Fe}^{2.5+}$  (Dyar et  
220 al. 2006). Despite this issue concerning the distribution of hyperfine parameters, an estimate  
221 for  $\text{Fe}^{3+}/\text{Fe}^{2+}$  ratio for the studied samples could be determined if D1 and D2 are associated to  
222  $\text{Fe}^{2+}$  and  $\text{Fe}^{3+}$ , respectively, based on the average values of hyperfine parameters as previously  
223 mentioned. Thus, considering the relative areas for D1 and D2 (Table 3),  $\text{Fe}^{3+}/\text{Fe}^{2+}$  ratio ranges  
224 from 0.282 (for sample PT2d) up to 0.857 (for sample J338-23).  $\text{Fe}^{3+}/\text{Fe}_{\text{total}}$  can be estimated  
225 between 22% (for PT2d) and 36% (for J338-23), taking  $\text{Fe}_{\text{total}} = \text{Fe}^{3+} + \text{Fe}^{2+}$ . The average  
226  $\text{Fe}^{3+}/\text{Fe}_{\text{total}}$  ratio is  $27.7 \pm 5.4\%$  for the three typical atacamaite samples (i.e. the ones with  
227 magnetic susceptibility between 176 and 272  $10^{-9} \text{ m}^3/\text{kg}$ , namely JG2h, PT2d, and K51f).  
228 These ratios are considerably higher than the ones already reported for tektites from other  
229 strewnfields, whose  $\text{Fe}^{3+}/\text{Fe}^{2+}$  (or  $\text{Fe}^{3+}/\text{Fe}_{\text{total}}$ ) ratios are close to zero (Dunlap and Sibley 2004;  
230 Giuli et al., 2002).

231

## 232 **6. Dating**

233 The fission-track dating method, applied successfully to a variety of impact glasses (e.g., Folco  
234 et al., 2011), was used on two samples collected 3 km apart. The plateau corrected fission-track  
235 ages (Storzer and Wagner, 1969) are  $8.08 \pm 0.54$  Ma and  $7.57 \pm 0.52$  Ma ( $\pm 1\sigma$ ), consistent within  
236  $1\sigma$  error, and with an average  $7.83 \pm 0.26$  Ma (Table 4).

237

## 238 **7. Discussion**

### 239 **7.1. Nature of atacamaïtes**

240 Petrological and geochemical characteristics of atacamaïtes, such as the occurrence of  
241 lechatelierite that evidence temperatures above  $1700^{\circ}\text{C}$  (Macris et al., 2014) and the low water  
242 content (below 200 ppm) exclude a volcanic origin and indicate formation by hypervelocity  
243 impact. Such high temperatures may also be reached naturally by lightning, but the  
244 morphology, texture and spatial repartition of atacamaïtes preclude that they are fulgurites.  
245 Compositions in major and trace elements, including the REE patterns, suggest a relatively  
246 homogeneous lithology for the target rocks, superimposed with a Fe, Ni, and Co extraterrestrial  
247 contamination (Fig. 3-5). Although atacamaïtes and local Andean dacites have whole rock, Sr  
248 and Nd isotopic compositions in the same ranges, no lava with exactly the same compositions  
249 has yet been identified in the existing database (Oliveiros et al., 2020).

### 250 **7.2. Impactor**

251 The enrichment in Ni and Co in atacamaïtes (2148 ppm and 182 ppm, respectively, on average,  
252 and up to 4800 ppm and 400 ppm in the most magnetic samples) compared to dacites, and the  
253 strong correlation between Fe, Ni and Co contents indicate a significant contamination by an

254 extraterrestrial impactor rich in Fe, Ni and Co (Fig. 3). Although we do not know the  
255 composition of the target, it is necessarily a dacitic rock that has practically no Ni and Co  
256 compared to the impactor. Therefore, the Ni/Co ratio of the impactor can be estimated from  
257 the Ni/Co ratio of the most impactor-rich atacamaïtes. This ratio, computed for atacamaïtes  
258 with Ni content above 2500 ppm is  $Ni/Co=12.0\pm 0.2$  ( $1\sigma$ ,  $n=5$ ). The Ni/Co ratio of the impactor  
259 ( $12.0\pm 0.2$ ) is inconsistent with a chondritic projectile characterized by Ni/Co ratios around 21  
260 (e.g., Wasson and Kallemeyn, 1988). Similarly, the absence of enrichment in Cr precludes a  
261 chondritic impactor (Fig. 3C). Therefore, the geochemical data point to an iron impactor. Under  
262 the reasonable assumption that Fe, Ni, and Co are the only significant elements in the impactor  
263 and mixing lines as exemplified in Figure 3, the bulk composition of the impactor is estimated  
264 to 94.15 wt.% Fe, 5.4 wt.% Ni, 0.45 wt.% Co.

265 The 5.4 wt.% Ni content and the 12.0 Ni/Co ratio of the impactor allow to constrain more  
266 precisely the nature of the impactor. The only iron meteorite groups with similar Ni content  
267 ( $<7.5$  wt.%) are IC, IIAB, and IIG groups with average Ni contents of  $6.50\pm 0.27$  wt.% ( $1\sigma$ ,  
268  $n=41$  analyses),  $5.70\pm 0.33$  wt.% ( $n=274$ ),  $4.53\pm 0.44$  wt.% ( $n=18$ ), respectively (Koblitz, 2005;  
269 Gattacceca et al., 2018, Wasson et al., 2007). The average Ni/Co ratio for IC, IIAB, and IIG  
270 meteorites are  $14.17\pm 0.68$  ( $n=20$ ),  $12.41\pm 0.75$  ( $n=156$ ),  $8.97\pm 0.79$  ( $n=8$ ), respectively (Koblitz,  
271 2005; Gattacceca et al., 2018; Wasson et al., 2007). The best fit is clearly with IIAB meteorites.  
272 In particular, no IC meteorite has  $Ni/Co < 13.4$ , and no IIG meteorite has  $Ni/Co > 10.8$ . Only two  
273 meteorites from of the IAB complex, out of 537 analyses, have Ni content below 6 wt.%, and  
274 only 5, out of 326 analyses, have  $Ni/Co < 13$  (Koblitz, 2005). Therefore, this group is not  
275 considered as a candidate impactor for the atacamaïtes. In conclusion, the IIAB iron group is  
276 the most likely candidate for the impactor that formed the atacamaïtes.

277 Assuming that all the Ni was provided by the meteorite, an average of 5 wt.% impactor  
278 contamination can be estimated for atacamaïtes (range 0.8 % to 9 %). This elevated

279 contamination level is in the same range as glasses from small size craters like the 45 m-  
280 diameter Kamil crater (Fazio et al., 2016) or the 120 m-diameter Wabar crater (Mittlefeld et  
281 al., 1992).

282

### 283 7.3. Nomenclature and petrogenesis

284 A number of criteria are used to differentiate tektites from other splash-form impact glasses  
285 (e.g., Koeberl, 1994). Atacamaites have similarities with tektites: a water content of  $177\pm 32$   
286 ppm that is similar to the content of  $140\pm 80$  ppm in tektites (Beran and Koeberl, 1997),  
287 distribution over a relatively large strewnfield (similar to ivoirite and belizite strewnfields,  
288 Table 1), absence of relict grains or mineral inclusion in most samples.

289 Atacamaites also have similarities with more proximal splash-form impact glasses. They show  
290 small-scale chemical heterogeneities due to a strong contamination by the impactor, while only  
291 minor contamination is reported in tektites.

292 The redox state of Fe determined by Mössbauer spectroscopy in 5 samples, including two very  
293 magnetic ones, yields a ratio of  $\text{Fe}^{3+}/\text{Fe}_{\text{total}}$  between 22% and 36% (average  $27.7\pm 5.4\%$  for the  
294 three typical samples). This  $\text{Fe}^{3+}/\text{Fe}_{\text{total}}$  ratio of  $27.7\pm 5.4\%$  show that atacamaites are also much  
295 more oxidized than tektites whose oxidation ratios are near zero (Table 1). Atacamaites contain  
296 Fe oxides inclusions more frequently than tektites where their occurrence is extremely rare. As  
297 a consequence, they are more magnetic than tektites, and their magnetic properties are more  
298 variable, especially for small specimens (Rochette et al., 2015).

299 Beside tektites *sensu stricto*, the occurrences of macroscopic splash-form impact glasses, are  
300 limited (Table 1). Millimeter-sized ballistic ejecta are found around the Wabar impact craters  
301 under the form of glassy droplets (Mittlefeldt et al., 1992), but these are limited to a few  
302 hundred meters around three small craters with maximum diameter 120 m (Gnos et al., 2013).

303 Glass with crude splash-forms is also found over limited areas on the rims of the 390 m-  
304 diameter Aouelloul crater (Koeberl et al., 1998). Centimeter-sized splash-form glasses are  
305 found over a much wider area (~400 km<sup>2</sup>) around the 1.2 km-diameter Darwin crater (Taylor  
306 and Solomon, 1962; Howard, 2009). The impact glasses with closest similarity to atacamaites  
307 are irghizites, associated with the 14 km-diameter Zhamanshin crater in Kazakhstan (Bouska  
308 et al., 1981). Irghizites and atacamaites share similar morphologies (including presence of  
309 small attached spherules, Fig. 2a), and important contamination by the impactor (Schulz et al.,  
310 2020). A significant difference is the extent of the strewnfield (1-2 km<sup>2</sup> for irghizites vs. 650  
311 km<sup>2</sup> for Atacamaites).

312 This inventory of tektites and other splash-form impact glasses (Table 1) confirms that it is  
313 necessary to combine a number of criteria to discriminate the two categories (following  
314 Koeberl, 1994). Chemical homogeneity is a tektite attribute, but it is hard to quantify this  
315 homogeneity, and tektites may be heterogeneous (e.g., North American ones, see Albin et al.,  
316 2000, and Muong Nong tektites, see Koeberl, 1992). Water content may be ambiguous as non-  
317 tektite glasses can be as dry as tektites (Table 1). The reduced character is not exclusive as  
318 well, as the Darwin glass is as reduced as tektites (e.g., Rochette et al. 2015). Another criterion  
319 may be the distance from the crater that is at least an order of magnitude higher for tektites, but  
320 this criterion cannot be strictly applied when the crater location is unknown. A final criterion  
321 is crater size, with tektites being associated to craters larger than 10 km. Both criteria cannot  
322 be used when the crater is missing, as for atacamaites. In fact, the only other cases of  
323 macroscopic non tektite impact glasses without known source crater are Libyan desert glass  
324 (e.g., Barrat et al., 1997), and urengoites (e.g., Deutsch et al., 1997), two glasses for which  
325 splashforms are not established. The smaller size range (the largest atacamaites are about the  
326 size of the smallest tektites) as well as presence of contorted shapes seems to be good criteria  
327 for non-tektite material. In addition to the oxidized character and the high impactor

328 contamination observed in atacamaites, this clearly precludes the classification of atacamaites  
329 as tektites.

#### 330 *7.4. Source impact crater*

331 Considering our fission track age for the atacamaites ( $7.83 \pm 0.26$  Ma) compared to erosion rates  
332  $< 1$  m/Ma measured in the hyper-arid part of the Atacama Desert (e.g., Dunai et al., 2005), a  
333  $\sim 10$  km diameter (Zhamanshin size) crater and the associated  $\sim 400$  m deep depression should  
334 still be visible in the field and on satellite images. On the other hand, published erosion rates  
335 were obtained on surfaces specially selected for their stable morphology. Areas with steep  
336 slope or low relative altitude may have higher erosion rates or may have accumulated post 8  
337 Ma sediments. Search for impact breccia or non-ejected impact glass were also inconclusive  
338 despite several weeks of field work. The failure to detect a candidate source crater for  
339 atacamaites suggests it may have been much smaller than 10 km, in the size range of Darwin  
340 crater (1.2 km diameter) that produced a  $\sim 400$  km<sup>2</sup> strewnfield with  $\sim 15\%$  of splash-form  
341 (Howard, 2009). Modeling shows that cm-sized particles for such small craters can indeed be  
342 ejected for several tens of km (Shuvalov and Dypvik, 2013). Finding such delicate glass ejecta  
343 present at the surface of Atacama Desert since nearly 8 Ma points toward the extreme stability  
344 of Atacama Desert surfaces, already demonstrated by elevated cosmogenic nuclide contents  
345 (Dunai et al., 2015), high meteorite densities (Hutzler et al., 2007), and old meteorite terrestrial  
346 ages (Drouard et al., 2019).

347

## 348 **8. Conclusions**

349 Atacamaites are cm-sized glassy splash-form ejecta found over at least 650 km<sup>2</sup> in the Central  
350 Depression of the Atacama Desert. They are the product of the fusion and ejection of local  
351 andesitic rocks by the hypervelocity impact of an iron meteoroid that occurred at  $\sim 7.8$  Ma. **The**

352 most likely nature of the impactor is the IIAB iron group. No source crater has been identified  
353 so far, despite its likely proximal location. Atacamaites do not qualify as tektites *sensu stricto*  
354 because of their smaller size, more oxidized character, and high contamination by the impactor.  
355 The discovery of atacamaites adds a new example of a significantly large strewnfield of ejected  
356 tektite-like glass that does not meet a number of criteria to qualify as tektite. Following  
357 Rochette et al. (2015), we propose to categorize such objects as “tektoids”, to shorten the  
358 description as “non tektite splash-form impact glasses” and to emphasize their similar aspect  
359 to tektites. Better understanding of the specificities of atacamaites should come from finding  
360 the source crater or from our ongoing exploration of the variability of atacamaites within their  
361 strewnfield (geochemistry, contamination level, size distribution, morphology, ...). The  
362 characteristics of atacamaites increase the diversity of known impact glasses and hold crucial  
363 information to further understand the mechanisms of formation of impact glasses in general,  
364 and the consequences of terrestrial impacts on the environment.

365

## 366 **ACKNOWLEDGMENTS**

367 We thank Luigi Folco and an anonymous reviewer for their useful and constructive comments  
368 that helped improve this manuscript. This project was funded by the Programme National de  
369 Planétologie (INSU/CNES), and FONDECYT (3140562). BR acknowledges financial support  
370 of the LABEX Lyon Institute of Origins (ANR-10-LABX-0066) of the Université de Lyon  
371 within the program "Investissements d'Avenir" (ANR-11-IDEX-0007) of the French  
372 government operated by the National Research Agency (ANR). The national Raman facility at  
373 ENS de Lyon is supported by INSU.

374

## 375 **FIGURE CAPTIONS**



376 **Fig. 1.** Map of atacamaite strewnfield. Its estimated limits are indicated by the solid line.  
377 Geological information is from Espinoza et al. (2012).

378 **Fig. 2.** Morphologies and petrography of atacamaites. (a) Macroscopic images. (b) Transmitted  
379 light image of a thick section evidencing compositional schlieren and bubbles. (c) Backscatter  
380 electron image of a sectioned typical atacamaite. (d) Transmitted plane polarized light image  
381 of a lechatelierite inclusion. (e) Backscatter electron image of Fe oxides in a highly magnetic  
382 atacamaite.

383 **Fig. 3.** Atacamaite geochemistry. Ni (a), Co (b), Cr (c) contents vs. Fe content. The linear fits  
384 are for ICP-AES data. The fields for pre-Pliocene lavas ( $\text{SiO}_2=60\text{-}70$  wt.%, from Oliveiros et  
385 al., 2020) are shown for comparison. Note that no Cr enrichment is apparent, consistent with  
386 an iron impactor.

387 **Fig. 4.** REE concentrations in 12 atacamaites. Concentrations are normalized to CI chondrites  
388 (Barrat et al., 2012).

389 **Fig. 5.** Sr and Nd isotopic compositions of atacamaites compared with those of pre-Pliocene  
390 Andean volcanics (Oliveiros et al., 2020).

391 **Fig. 6.** (a) Room temperature  $^{57}\text{Fe}$  Mössbauer spectrum for atacamaite sample PT7b. (b) Three-  
392 dimensional representation of the total probability distribution  $P(\delta, \Delta)$  for PT7B sample as  
393 obtained by means of x-VBF method. (c) Contour plots in isomer shift ( $\delta$ ), quadrupole splitting  
394 ( $\Delta$ ) plane. For  $P(\delta, \Delta) < 0.55$ , the contour lines are shown as solid lines. For  $P(\delta, \Delta) > 0.55$ , the  
395 contour lines are shown as broken lines. All lines are spaced at intervals of 0.11.

396

## 397 References

398 Albin, E.F., Norman, M.D., Roden, M. 2000. Major and trace element compositions of  
399 georgiites : clues to the source of North American tektites. *Meteorit. Planet. Sci.* 35, 795–  
400 806.

401 Anders, E., Grevesse, N., 1989. Abundances of the elements: meteoritic and solar. *Geochim.*  
402 *Cosmochim. Acta* 53, 197–214.

403 Barrat, J.-A., Jahn, B.M., Amossé, J., Rocchia, R., Keller, F., Poupeau, G.R., Diemer, E., 1997.

404 Geochemistry and origin of Libyan Desert glasses. *Geochim. Cosmochim. Acta* 61, 1953–

405 1959.

406 Barrat, J.-A., Zanda, B., Moynier, F., Bollinger, C., Liorzou, C., Bayon, G., 2012.  
407 Geochemistry of CI chondrites: Major and trace elements, and Cu and Zn isotopes.  
408 *Geochim. Cosmochim. Acta* 83, 79–92.

409 Barrat, J.-A., Dauphas, N., Gillet, P., Bollinger, C., Etoubleau, J., Bischoff, A., Yamaguchi,  
410 A., 2016. Evidence from Tm anomalies for non-CI refractory lithophile element  
411 proportions in terrestrial planets and achondrites. *Geochim. Cosmochim. Acta*, 176, 1–17.

412 Beran, A., Koeberl, C., 1997. Water in tektites and impact glasses by Fourier-transform  
413 infrared spectroscopy. *Meteorit. Planet. Sci.* 32, 211–216.

414 Bigazzi, G., De Michele, V., 1996. New fission-track age determinations on impact glasses.  
415 *Meteorit. Planet. Sci.* 31, 234–236.

416 Bouska, V., Povondra, P., Florenskij, P.V., Randa, Z., 1981. Irghizites and Zhamanshinites:  
417 Zhamanshin crater, USSR. *Meteoritics* 16, 171–1884.

418 Braukmüller, N., Wombacher, F., Heze, D.C., Escoube, R., Münker, C., 2018. The chemical  
419 composition of carbonaceous chondrites: Implications for volatile element depletion,  
420 complementarity and alteration. *Geochim. Cosmochim. Acta*. 239, 17–48.

421 Chao, E.C.T., Dwornik, E.J., Merrill, C.W., 1966. Nickel-iron spherules from Aouelloul glass.  
422 *Science* 154, 759–760+765.

423 Cornell, R.M., Schwertmann, U., 2003. The iron oxides: structure, properties, reactions,  
424 occurrences and uses. Weinheim, Germany: Wiley-VCH Verlag GmbH & Co. KgaA.

425 Cotten, J., Le Dez, A., Bau, M., Caroff, M., Maury, R., Dulski, P., Fourcade, S., Bohn, M.,  
426 Brousse, R., 1995. Origin of rare-earth element and yttrium enrichments in subaerial  
427 exposed basalts: evidence from French Polynesia. *Chemical Geol.* 119, 115–138.

428 Deutsch, A., Ostermann, M., Masaitis, V.L., 1997. Geochemistry and neodymium-strontium  
429 isotope signature of tektite-like objects from Siberia (urengoites, South-Ural glass).  
430 *Meteorit. Planet. Sci.* 32, 679–686.

431 Dressler, B.O., Reimold, W.U., 2001. Terrestrial impact melt rocks and glasses. *Earth Sci. Rev.*  
432 56, 205-284.

433 Drouard, A., Gattacceca, J., Hutzler, A., Rochette, P., Braucher, R., Boursières, D., ASTER Team,  
434 Gounelle, M., Morbidelli, A., Debaille, V., Van Ginneken, M., Valenzuela, M., Quesnel,

435 Y., Martinez, R., 2019. The meteorite flux of the past 2 m.y. recorded in the Atacama  
436 Desert. *Geology* 47, 673–676.

437 Dunlap, R.A., Sibley, A.D.E., 2004. A Mössbauer effect study of Fe-site occupancy in  
438 Australasian tektites. *J. Non-Crystalline Solids* 337, 36–41.

439 Dunlap, R.A., McGraw, J.D., 2007. A Mössbauer effect study of Fe environments in impact  
440 glasses. *J. Non-Crystalline Solids* 353, 2201–2205.

441 Dyar, M.D., Agresti, D.G., Schaefer, M.W., Grant, C.A., Sklute, E.C., 2006. Mössbauer  
442 spectroscopy of earth and planetary materials. *Annual Rev. Earth and Planet. Sci.* 34, 83-  
443 125.

444 Espinoza, F.G., Matthews, S.J., Cornejo P.P., 2012. Carta Los Vientos, Región de Antofagasta.  
445 Servicio Nacional de Geología y Minería, Carta Geológica de Chile, Serie Geología Básica  
446 138: 72 p., scale 1:100.000. Santiago.

447 Fazio, A., D'Orazio, M., Cordier, C., Folco, L., 2016. Target-projectile interaction during  
448 impact melting at Kamil Crater, Egypt. *Geochim. Cosmochim. Acta* 180, 33–50.

449 Folco, L., Bigazzi, G., D'Orazio, M., Balestrieri, M.L., 2011. Fission track age of  
450 Transantarctic Mountain microtektites. *Geochim. Cosmochim. Acta* 75, 2356–2360.

451 Gattacceca, J., Bouvier, A., Grossman, J., Metzler, K., Uehara, M. 2018. The Meteoritical  
452 Bulletin, No 106. *Meteorit. Planet. Sci.* 54, 469–471.

453 Gentner, W., Storzer, D. Wagner, G.A., 1969. New fission track ages of tektites and related  
454 glasses. *Geochim. Cosmochim. Acta* 33, 1075–1081.

455 Giuli, G., Pratesi, G., Cipriani, C., Paris, E., 2002. Iron local structure in tektites and impact  
456 glasses by extended X-ray absorption fine structure and high-resolution X-ray absorption  
457 near-edge structure spectroscopy. *Geochim. Cosmochim. Acta* 66, 4347–4353.

458 Gnos, E., Hofmann, B.A., Halawani, M.A., Tarabulsi, Y., Hakeem, M., Al Shanti, M., Greber,  
459 N.D., Holm, S., Alwmark, C., Greenwood, R.C., Ramseyer, K., 2013. The Wabar impact  
460 craters, Saudi Arabia, revisited. *Meteorit. Planet. Sci.* 48, 2000–2014.

461 Haines, P.W., Jenkins, R.J., Kelley, S.P., 2001. Pleistocene glass in the Australian desert: the  
462 case for an impact origin. *Geology* 29, 899–902.

463 Howard, K.T., 2009. Physical distribution trends in Darwin glass. *Meteorit. Planet. Sci.* 44,  
464 115–129.

465 Hutzler, A., Gattacceca, J., Rochette, P., Braucher, R., Carro, B., Christensen, E., Cournède,  
466 C., Gounelle, M., Laridhi-Ouazaa, N., Martinez, R., Warner, M., Bourlès, D., 2016.  
467 Description of a very dense meteorite collection area in western Atacama: insight into the  
468 long-term composition of the meteorite flux to Earth. *Meteorit. Planet. Sci.* 51, 468–482.

469 Johnson, J.A., Johnson, C.E., 2005. Mössbauer spectroscopy as a probe of silicate glasses. *J.*  
470 *Physics: Condensed Matter* 17, R381–R412.

471 Koeberl, C. 1992. Geochemistry and origin of Muong Nong-type tektites. *Geochim.*  
472 *Cosmochim. Acta* 56:1033–1064.

473 Koeberl, C., 1994. Tektite origin by hypervelocity asteroidal or cometary impact. Target rocks,  
474 source craters, and mechanisms, *in* Dressler, B.O., Grieve, R.A.F., and Sharpton, V.L.,  
475 eds., *Large Meteorite Impacts and Planetary Evolution: Geological Society of America*  
476 *Special Paper* 293, p. 133-152.

477 Koeberl, C., 2014. The Geochemistry and Cosmochemistry of Impacts, in *Planets, Asteroids,*  
478 *Comets and The Solar System*, *in* Andrew M. Davis, ed., *Treatise on Geochemistry*  
479 (Second Edition), v. 2, p.73-118.

480 Koeberl, C., Bottomley, R., Glass, B.P., Storzer, D., 1997. Geochemistry and age of Ivory  
481 Coast tektites and microtektites. *Geochim. Cosmochim. Acta* 61, 1745–1772.

482 Koeberl, C., Reimold, W.U., Shirey, S.B., 1998. The Aouelloul crater, Mauritania: on the  
483 problem of confirming the impact origin of a small crater. *Meteorit. Planet. Sci.* 33, 513–  
484 517.

485 Koeberl, C., Crosta, A.P., Schulz, T., 2019. Geochemical investigation of the atacamaites, a  
486 new impact glass occurrence in South America. *50<sup>th</sup> Lunar Planet. Sci. Conf.*, abstract  
487 1255.

488 Koblitz, J. 2005. MetBase – Meteorite Data Retrieval Software, version 7.1. Bremen, Germany  
489 (CD-ROM).

490 Lagarec, K., Rancourt, D.G. 1997. Extended Voigt-based analytic lineshape method for  
491 determining N-dimensional correlated hyperfine parameter distributions in Mössbauer  
492 spectroscopy. *Nuclear Instruments Methods Phys. Res. Section B* 126, 266–280.

493 Laurenzi, A., Balestrieri, M.L., Bigazzi, G., Hadler Neto, J.C., Iunes, P.J., Norelli, P., Oddone,  
494 M., Osorio Araya, A.M., Viramonte, J.G., 2007. New constraints on ages of glasses  
495 proposed as reference materials for fission-track dating. *Geostandards Geoanalytical Res.*  
496 31, 105–124.

497 Macris, C.A., Asimow, P.D., Badro, J., Eiler, J.M., Zhang, Y., Stolper, E.M., 2018. Seconds  
498 after impact: Insights into the thermal history of impact ejecta from diffusion between  
499 lechatelierite and host glass in tektites and experiments. *Geochim. Cosmochim. Acta* 241,  
500 69–94.

501 Magna, T., Zak, K., Pack, A., Moynier, F., Mougél, B., Peters, S., Skala, R., Jonasova, S.,  
502 Mizera, J., Randa, Z., 2017. Zhamanshin astrobleme provides evidence for carbonaceous  
503 chondrite and post-impact exchange between ejecta and Earth's atmosphere. *Nature*  
504 *Communications* 88, article no. 227.

505 Murali, A.V., Zolensky, M.E., Blanchard, D.P., 1987. Tektite-Like Bodies at Lonar Crater,  
506 India, Implications for the Origin of Tektites. *J. Geophys. Res.* 92, no. B4, E729–E735.

507 Mittlefehldt, D.W., See, T.H., Hörz, F., 1992. Dissemination and fractionation of projectile  
508 materials in the impact melts from Wabar Crater, Saudi Arabia. *Meteoritics* 27, 361–370.

509 Oliveros, V., Moreno-Yaeger, P., Flores, L., 2020. Igneous Rock Associations 25. Pre-Pliocene  
510 Andean Magmatism in Chile. *Geoscience Canada*, 47, 65–82.

511 Osinski, G.R., Kieniewicz, J., Smith, J.R., Boslough, M., Eccleston, M., Scharcz, H.P.,  
512 Kleindienst, M.R., Haldemann, A.F.C., Churcher, C.S., 2008. The Dakhleh Glass: Product  
513 of an impact airburst or cratering event in the Western Desert of Egypt? *Meteorit. Planet.*  
514 *Sci.* 43, 2089–2107.

515 Rochette, P., Gattacceca, J., Devouard, B., Moustard, F., Bezaeva, N., Cournède, C., Scaillet,  
516 B., 2015. Magnetic properties of tektites and other related impact glasses. *Earth Planet.*  
517 *Sci. Lett.* 432, 381–390.

518 Rochette, P., Bezaeva, N., Kosterov, A., Gattacceca, J., Masaitis, V., Badyukov, D.D., Giuli,  
519 G., Lepore, G.O., Beck, P., 2019. Magnetic Properties and Redox State of Impact Glasses:  
520 A Review and New Case Studies from Siberia. *Geosciences* 9, article no. 225.

521 Rochette, P., Beck, P., Braucher, R., Cornec, J., Debaille, V., Devouard, B., Gattacceca, J.,  
522 Jourdan, F., Moustard, F., Moynier, F., Nomade, S., Reynard, B., 2021. A new tektite  
523 strewn-field and source crater couple discovered in Central America: insights into the  
524 tektite generation process and its ubiquity. *Commun. Earth Environ.* 2, 94.  
525 Doi:10.1038/s43247-021-00155-1.

526 Roperch, P., Gattacceca, J., Valenzuela, M., Devouard, B., Lorand, J.-P., Arriagada, C.,  
527 Rochette, P., Latorre, C., Beck, P., 2017. Surface vitrification caused by natural fires in  
528 Late Pleistocene wetlands of the Atacama desert. *Earth and Planetary Science Letters* 469,  
529 15–26.

530 Rossano, S., Balan, E., Morin, G., Bauer, J.P., Calas, G., Brouder, C., 1999.  $^{57}\text{Fe}$  Mössbauer  
531 spectroscopy of tektites. *Phys. Chem. Minerals* 26, 530–538.

532 Sandhu, A.S., Westgate, J.A., Alloway, B.V., 1993. Optimizing the isothermal plateau fission-  
533 track dating method for volcanic glass shards. *Nuclear Tracks Radiation Measurements*  
534 21, 479–488.

535 Schulz, T., Sackl, F., Fragner, E., Luguët, A., van Acken, D., Begosew, A., Badyukov, D.D.,  
536 Koeberl, C., 2020. The Zhamanshin impact structure, Kazakhstan: A comparative  
537 geochemical study of target rocks and impact glasses. *Geochim. Cosmochim. Acta* 268,  
538 209–229.

539 Schultz, P.H., Zárata, M., Hames, B., Koeberl, C., Bunch, T., Storzer, D., Renne, P., Wittke,  
540 J., 2004. The Quaternary impact record from the Pampas, Argentina. *Earth Planet. Sci.*  
541 *Lett.* 219, 221–238.

- 542 Shuvalov, V., Dypvik, H., 2013, Distribution of ejecta from small impact craters. *Meteorit.*  
543 *Planet. Sci.* 48, 1034–1042.
- 544 Stewart, S.J., Cernicchiaro, G., Scorzelli, R.B., Poupeau, G., Acquafredda, P., De Francesco,  
545 A., 2003. Magnetic properties and  $^{57}\text{Fe}$  Mössbauer spectroscopy of Mediterranean  
546 prehistoric obsidians for provenance studies. *J.Non-Crystalline Solids* 323, 188–192.
- 547 Storzer, D., Wagner, G.A., 1970. Fission track ages and ages of deposition of deep-sea  
548 microtektites. *Science* 168, 359–361.
- 549 Storzer, D., Poupeau, G., 1973. Ages-plateau de minéraux et verres par la méthode des traces  
550 de fission. *C. R. de l'Académie des Sciences Paris* 276 (D), 317–319.
- 551 Storzer, D., Wagner, G.A., 1969. Correction of thermally lowered fission-track ages of tektites.  
552 *Earth Planet. Sci. Letters* 5, 463–468.
- 553 Taylor, S.R., Solomon, M., 1962. Geochemical and geological evidence for the origin of  
554 Darwin glass. *Nature* 196, 124–126.
- 555 Wasson, J.T., Kallemeyn, G.W., 1988. Compositions of chondrites. *Philosoph. Transactions*  
556 *Royal Society London* A325, 535–544.
- 557 Wasson, J.T., Huber, H., Malvin, D.J., 2007. Formation of IIAB iron meteorites. *Geochim.*  
558 *Cosmochim. Acta* 71, 760–781.

560 **Table 1.** Characteristics of known splash-form impact glasses.

	Fe <sup>3+</sup> /Fe <sub>total</sub>	water (ppm)	magnetic susceptibility (10 <sup>-9</sup> m <sup>3</sup> /kg)		maximum distance from crater (km)	crater diameter (km)	age (Ma)	impactor
			mean±SD	range				
Australasian*	<0.1	156±76	82±10	73-129	≥5000	?	0.788	ordinary chondrite?
belizites*	<0.1	99±31	127±5	112-193	530	14	0.8	ordinary chondrite
ivoirites*	<0.1	23±5	103±12	62-138	320	10.5	1.1	L ordinary chondrite
moldavites*	<0.1	83±17	31±19	25-60	600	24	14.9	achondrite?
North-American*	<0.1	183±77	65±24	43-129	2300	85	35.5	chondrite?
Wabar glass	0.2	?	468±58	125-1025	1.3	0.12	0.005	IIIAB
Darwin glass	<0.1	470	53±23	34-79	35	1.2	0.73	?
irghizites	0.2-0.4	283±173	164±59	45-3320	0	13.5	0.9	carbonaceous chondrite
Aouelloul glass	0.3	350±20	82±9	38-463	0	0.36	3.1	Iron (IIB, IIID?)
<b>atacamaites</b>	<b>0.28±0.05</b>	<b>177±32</b>	<b>191±71</b>	<b>84-20500</b>	<b>≥50</b>	<b>?</b>	<b>7.6</b>	<b>Iron (IIAB)</b>

561 Tektites, indicated by \*, and other glasses are listed by increasing age. Other glasses are by  
562 alphabetical order. Non-ejected glasses tentatively attributed to impact or airbursts such as  
563 Dahkleh (Osinski et al., 2008), Argentinian (Schultz et al., 2004), and Edeowie glasses (Haines  
564 et al., 2001) are not listed, also because an alternative formation mechanism by fire and  
565 associated surface melting has been proposed for such glasses (Roperch et al., 2017). Magnetic  
566 properties from Rochette et al. (2015). Crater diameters, age, maximum distance and impactor  
567 type are mostly from Dressler and Reimold (2001) and Koeberl (2014). Fe<sup>3+</sup>/Fe<sub>total</sub> are from  
568 Rochette et al. (2019). Water content are mostly from Beran and Koeberl (1997). Other  
569 references used: Howard (2009) for Darwin glass, Gnos et al. (2013) for Wabar glass, Magna  
570 et al. (2017) for irghizites, Rochette et al. (2021) for belizites.



571 **Table 2.** Major and trace element abundances of atacamaites (oxides in wt.%, others in ppm).

#	K48k	K51j	K51f	JG2h	PT7e	PT3i	JG2a	PT7b	K51b	PT3b	PT2d	PT2g
$\chi$	188	133	272	176	91	1038	136	3593	167	168	132	147
SiO <sub>2</sub> *	64.3	66.4	60.1	64.5	68.1	58.2	65.8	60.2	64.1	64.7	66.2	66.3
TiO <sub>2</sub>	0.52	0.53	0.54	0.52	0.54	0.64	0.52	0.50	0.52	0.52	0.52	0.52
Al <sub>2</sub> O <sub>3</sub>	12.72	12.99	13.28	12.51	13.36	15.91	12.89	12.13	12.83	12.54	12.84	12.67
FeO	9.09	6.88	11.89	9.27	4.58	9.64	7.06	14.18	9.38	8.87	7.28	7.40
MnO	0.08	0.08	0.08	0.07	0.08	0.10	0.08	0.07	0.08	0.08	0.07	0.07
MgO	1.91	1.84	1.45	1.98	2.44	2.06	1.98	1.53	1.95	1.91	1.99	1.96
CaO	4.45	4.32	5.57	4.34	4.45	5.37	4.64	4.87	4.34	4.43	4.36	4.35
Na <sub>2</sub> O	3.58	3.60	3.54	3.52	3.37	4.12	3.71	3.19	3.47	3.56	3.53	3.57
K <sub>2</sub> O	2.91	3.06	2.94	2.91	2.97	3.55	3.05	2.67	2.88	2.98	2.89	2.89
P <sub>2</sub> O <sub>5</sub>	0.10	0.09	0.07	0.08	0.06	0.09	0.06	0.08	0.07	0.10	0.07	0.06
Co	224	133	311	222	45	208	144	409	217	212	150	159
Ni	2735	1545	3838	2636	412	2242	1703	4803	2584	2550	1697	1780
Li	49.34	53.38	56.46	49.86	52.77	64.29	48.11	46.57	46.65	50.66	48.14	48.85
Be	1.96	2.10	2.12	1.96	2.14	2.55	1.92	1.78	1.86	1.99	1.95	1.99
Sc	9.73	9.85	9.76	9.66	10.02	11.46	9.26	8.82	9.50	9.88	9.62	9.58
V	85.58	83.73	86.29	83.25	75.67	91.17	81.14	74.77	80.81	89.26	79.34	81.44
Cr	34.38	27.06	30.11	35.02	18.77	29.25	27.99	29.47	32.28	34.03	27.45	28.64
Cu	14.29	12.19	16.77	11.88	3.78	13.15	12.06	15.24	12.27	17.11	10.29	12.10
Zn	10.41	7.07	10.81	6.15	3.93	9.51	5.96	8.78	7.03	12.87	6.63	7.36
Ga	14.36	12.36	16.10	12.34	7.46	13.73	13.14	14.33	12.85	16.07	11.78	12.37
Rb	97.66	98.71	99.40	90.15	83.82	112.62	94.86	84.68	91.76	102.95	92.60	95.04
Sr	226	231	255	214	228	283	220	227	221	230	214	223
Y	38.74	39.78	38.54	38.37	41.52	47.67	37.45	33.99	37.63	39.59	38.34	38.66
Zr	178	178	195	172	175	231	167	167	168	180	169	172
Nb	11.41	11.13	11.83	11.03	11.55	13.56	10.66	10.30	10.62	11.38	10.77	10.91
Cs	5.48	5.28	4.98	4.89	4.25	5.71	6.26	5.29	5.96	6.81	5.95	6.02
Ba	635	650	631	616	723	769	623	589	624	652	552	633
La	37.12	38.35	36.30	36.67	41.85	45.59	36.61	33.35	36.70	38.45	36.90	37.60
Ce	69.61	74.78	72.30	69.17	77.76	88.96	69.59	65.65	69.13	73.32	70.12	70.82
Pr	8.18	8.86	8.40	8.30	9.18	10.35	8.34	7.60	8.26	8.73	8.32	8.47
Nd	31.79	34.39	32.79	32.33	35.22	40.82	32.42	29.40	32.22	33.92	32.44	32.81
Sm	6.67	6.94	6.77	6.68	7.45	8.38	6.61	6.03	6.63	7.01	6.67	6.74
Eu	1.09	1.07	1.07	1.08	1.13	1.31	1.05	0.95	1.07	1.12	1.06	1.08
Gd	6.53	6.14	6.12	6.30	6.71	7.60	6.12	5.52	6.19	6.54	6.27	6.25
Tb	1.02	0.96	0.95	0.98	1.05	1.19	0.96	0.87	0.97	1.02	0.98	0.99
Dy	6.09	5.84	5.70	5.98	6.54	7.16	5.79	5.29	5.92	6.26	5.99	6.00
Ho	1.24	1.22	1.18	1.24	1.37	1.50	1.20	1.10	1.23	1.30	1.25	1.26
Er	3.52	3.53	3.42	3.58	4.01	4.31	3.51	3.21	3.55	3.70	3.59	3.59

Yb	3.37	3.60	3.42	3.48	3.86	4.33	3.47	3.19	3.44	3.61	3.50	3.52
Lu	0.49	0.54	0.50	0.51	0.56	0.63	0.51	0.47	0.50	0.53	0.51	0.51
Hf	4.89	5.38	5.71	4.98	5.20	6.62	5.09	4.99	4.97	5.32	5.04	5.04
Ta	0.88	0.95	0.99	0.89	0.94	1.15	0.90	0.86	0.87	0.94	0.89	0.89
Pb	3.12	2.25	2.92	1.65	1.25	2.52	2.09	1.66	2.42	2.65	1.70	1.90
Th	11.42	10.98	11.41	11.25	12.28	13.73	11.21	10.70	11.36	12.21	11.43	11.35
U	1.91	1.80	1.51	1.92	1.73	1.92	1.92	1.39	1.87	2.18	1.85	1.83

572  $\chi$ : magnetic susceptibility in  $10^{-9} \text{ m}^3/\text{kg}$ . \*SiO<sub>2</sub> was not measured and obtained by difference  
573 assuming a total of 100 wt.%.

574

575

576 **Table 3.** Room temperature  $^{57}\text{Fe}$  hyperfine parameters for atacamaite samples

Samples	D1			D2			Magnetite								Area ratio D2/D1		
	$\langle\delta\rangle$ (mm/s)	$\langle\Delta\rangle$ (mm/s)	A (%)	$\langle\delta\rangle$ (mm/s)	$\langle\Delta\rangle$ (mm/s)	A (%)	Fe-A				Fe-B						
							$\langle\delta\rangle$ (mm/s)	$\langle\Delta\rangle$ (mm/s)	$\langle B_{\text{hf}}\rangle$ (T)	A (%)	$\langle\delta\rangle$ (mm/s)	$\langle\Delta\rangle$ (mm/s)	$\langle B_{\text{hf}}\rangle$ (T)	A (%)			
PT7b	1.02	2.07	64	0.52	0.83	36	-	-	-	-	-	-	-	-	-	-	0.56
JG2h	1.00	2.00	74	0.56	0.80	26	-	-	-	-	-	-	-	-	-	-	0.35
PT2d	0.99	1.95	78	0.53	0.79	22	-	-	-	-	-	-	-	-	-	-	0.28
K51f	0.93	2.10	65	0.53	0.76	35	-	-	-	-	-	-	-	-	-	-	0.54
J338-23	0.88	2.19	42	0.49	0.78	36	0.32	-0.01	48.6	14	0.70	-0.08	44.7	8	-	-	0.86

578

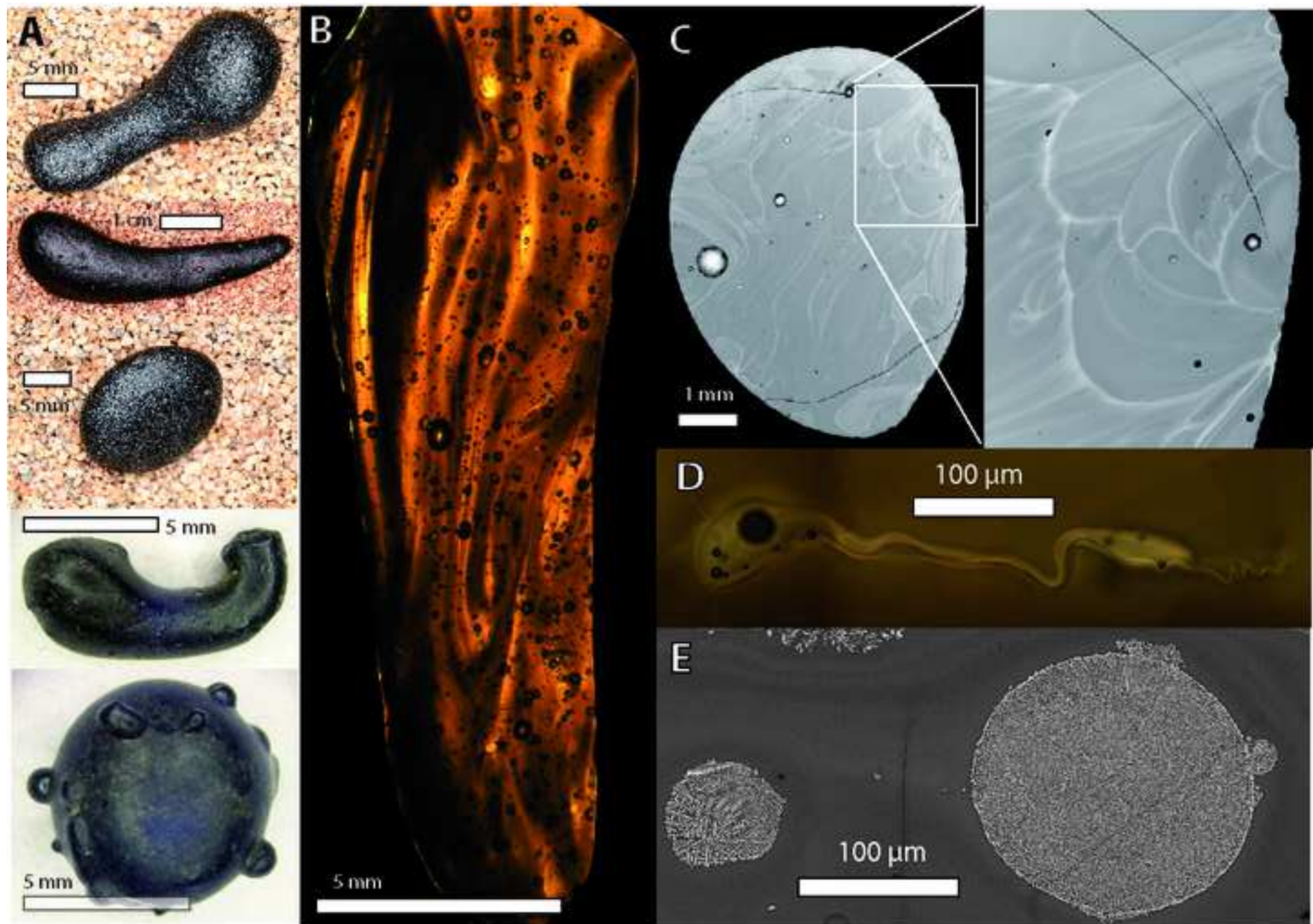
579  $\langle\delta\rangle$ : mean isomer shift relative to alpha-iron,  $\langle\Delta\rangle$ : mean quadrupole splitting,  $\langle B_{\text{hf}}\rangle$ : mean  
580 hyperfine field, A: relative area. The Gaussian widths for the center shift ( $\sigma_{\delta}$ ) and quadrupole  
581 splitting ( $\sigma_{\Delta}$ ) distributions range from 0.15 to 0.30 and 0.15 to 0.43, respectively. The  
582 correlation parameter for the x-VBF method are taken to be 0.01 and 0.07 for the D1 and D2  
583 distributions, respectively. Typical uncertainties for  $\langle\delta\rangle$ ,  $\langle\Delta\rangle$ , and  $\langle B_{\text{hf}}\rangle$  are  $\pm 2$  for the last  
584 digit. For relative area, uncertainty is  $\pm 1\%$ .

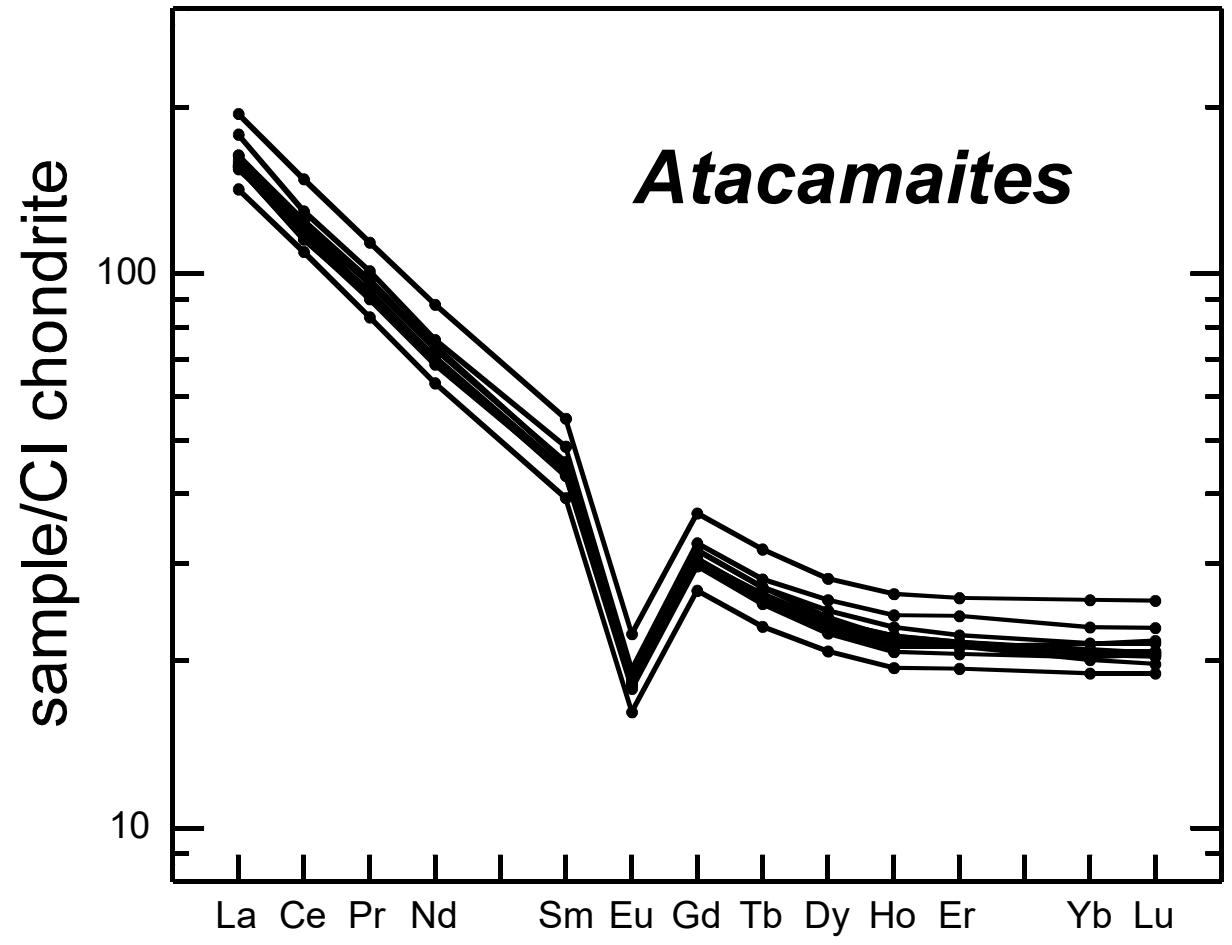
585

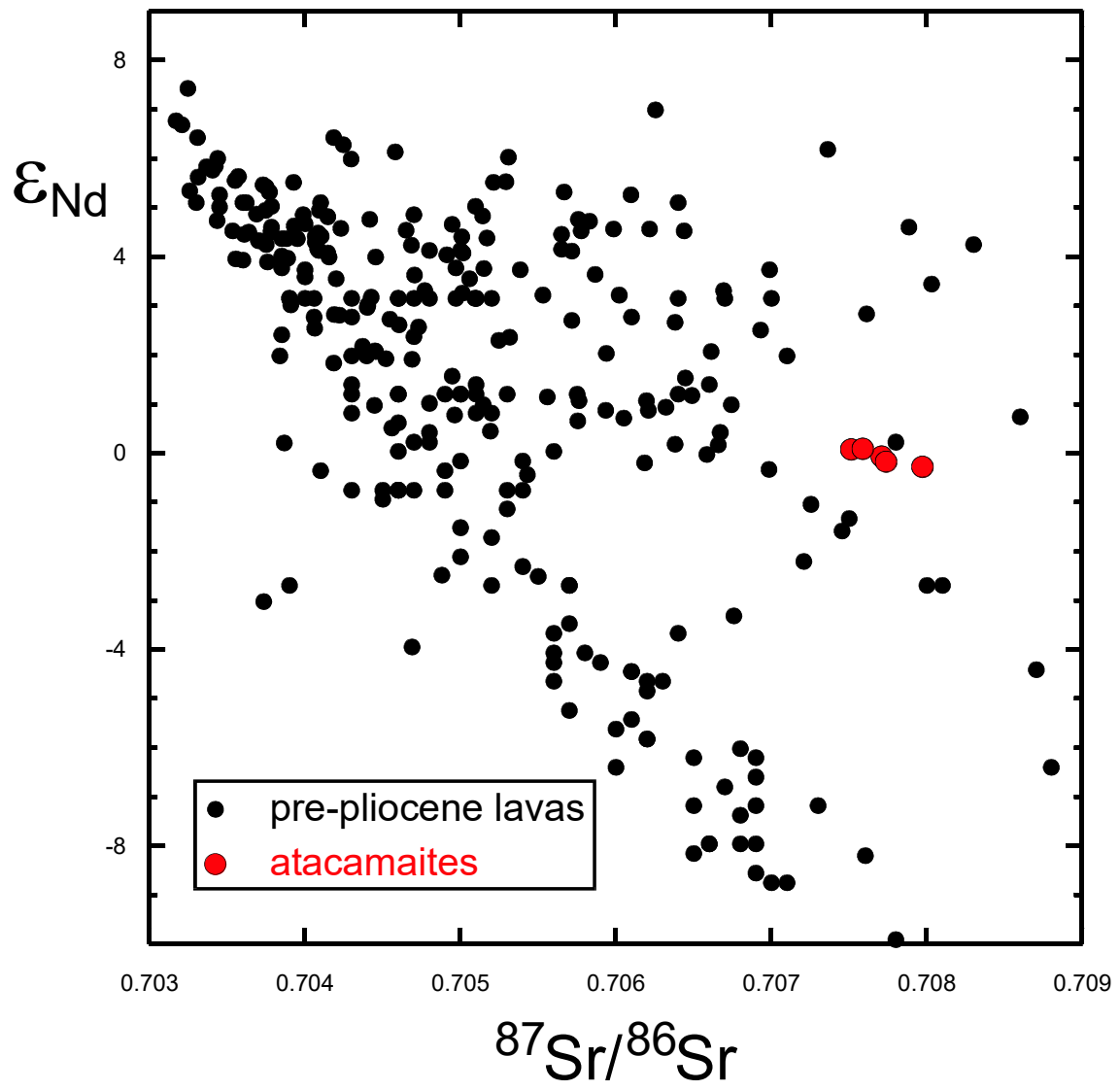
586 **Table 4.** Fission-track dating

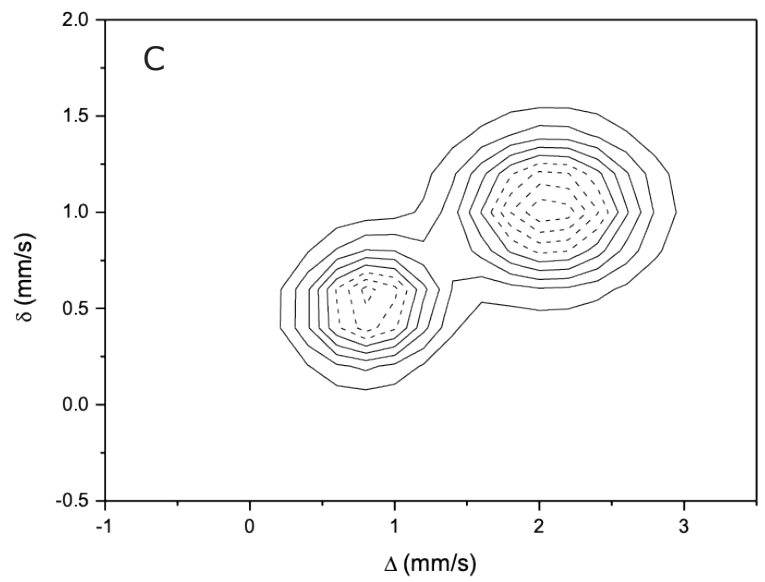
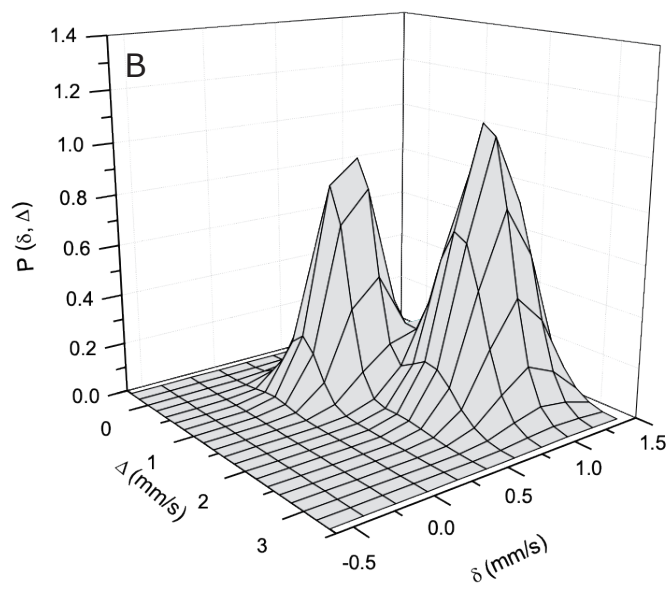
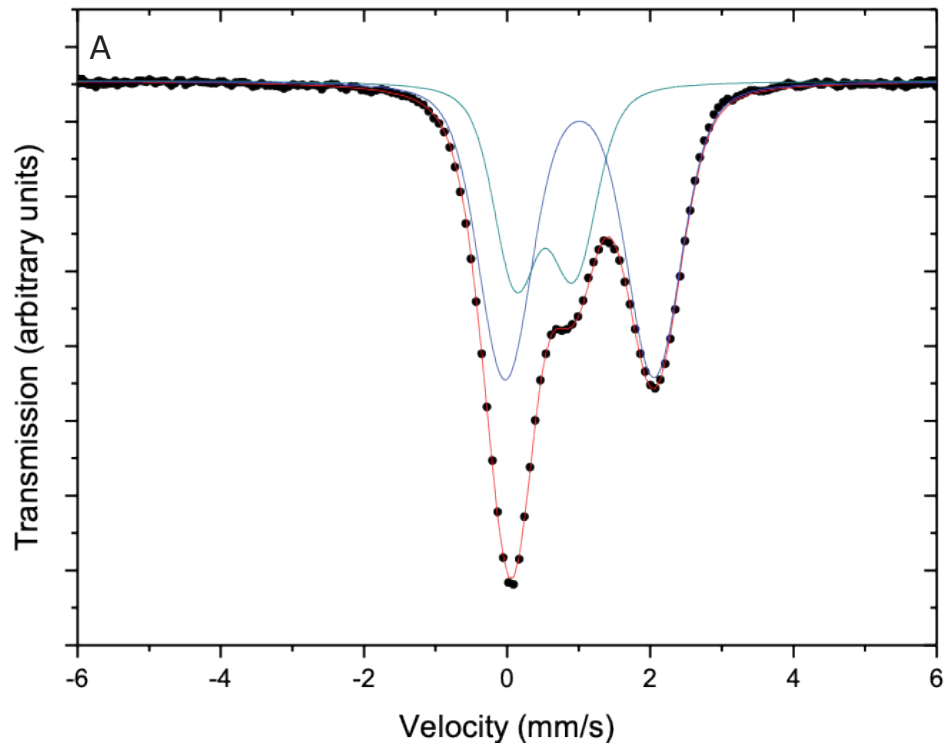
Sample	Heating	$\rho_s$ ( $\text{cm}^{-2}$ )	$n_s$	$\rho_i$ ( $\text{cm}^{-2}$ )	$n_i$	$p(\chi^2)$ (%)	$D_s/D_i$	Age ( $\pm 1\sigma$ ) (Ma)
JG26	Ambient	1990	66	183000	1071	66	0.72	$3.42 \pm 0.43$
	4h 220°C	1400	282	54700	1084	7	1.01	$8.08 \pm 0.54$
PT7E	Ambient	2370	329	177000	1041	99	0.83	$4.20 \pm 0.27$
	4h 220°C	1680	260	70100	1108	60	0.97	$7.57 \pm 0.52$

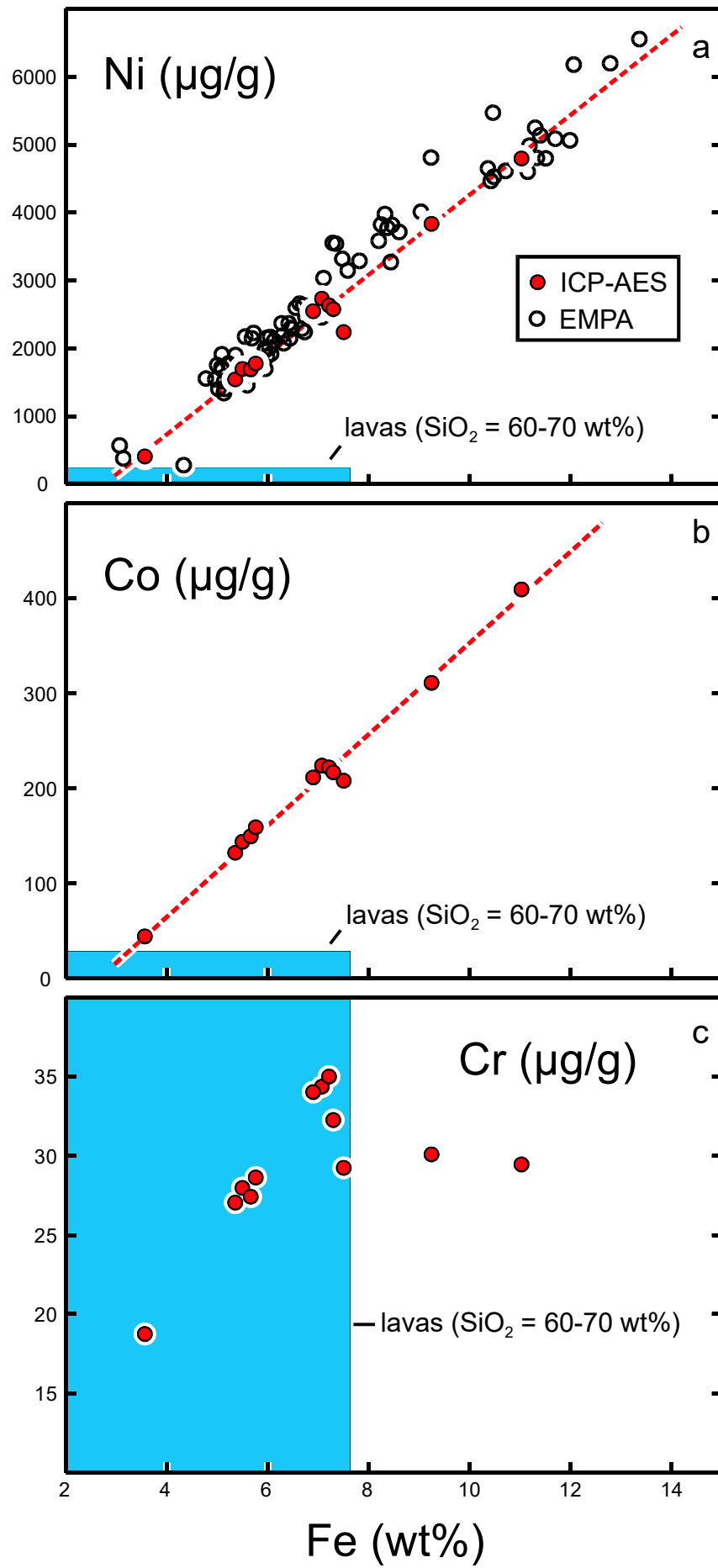
587 Heating: Thermal treatment imposed for plateau age determination;  $\rho_s$  ( $\rho_i$ ): spontaneous  
588 (induced) track density;  $n_s$  ( $n_i$ ): spontaneous (induced) tracks counted;  $p(\chi^2)$ : probability of  
589 obtaining  $\chi^2$  value testing induced track counts against a Poisson distribution;  $D_s/D_i$ :  
590 spontaneous to induced track-size ratio. Parameters used for age calculation:  $\lambda = 1.55125 \times 10^{-10}$   
591  $\text{a}^{-1}$ ;  $\lambda_F = 8.46 \times 10^{-17} \text{a}^{-1}$ ;  $\sigma = 5.802 \times 10^{-22} \text{cm}^2$ ;  $^{238}\text{U}/^{235}\text{U} = 137.88$ . Samples were irradiated  
592 in the Lazy Susan (Cd ratio 6.5 for Au and 48 for Co) facility of the Triga Mark II reactor of  
593 L.E.N.A., University of Pavia, Italy. The neutron fluence,  $\Phi = 5.26 \times 10^{15} \text{cm}^{-2}$ , was  
594 determined using the NRM IRMM-540 standard glass. Age errors are propagation of Poisson  
595 counting errors.



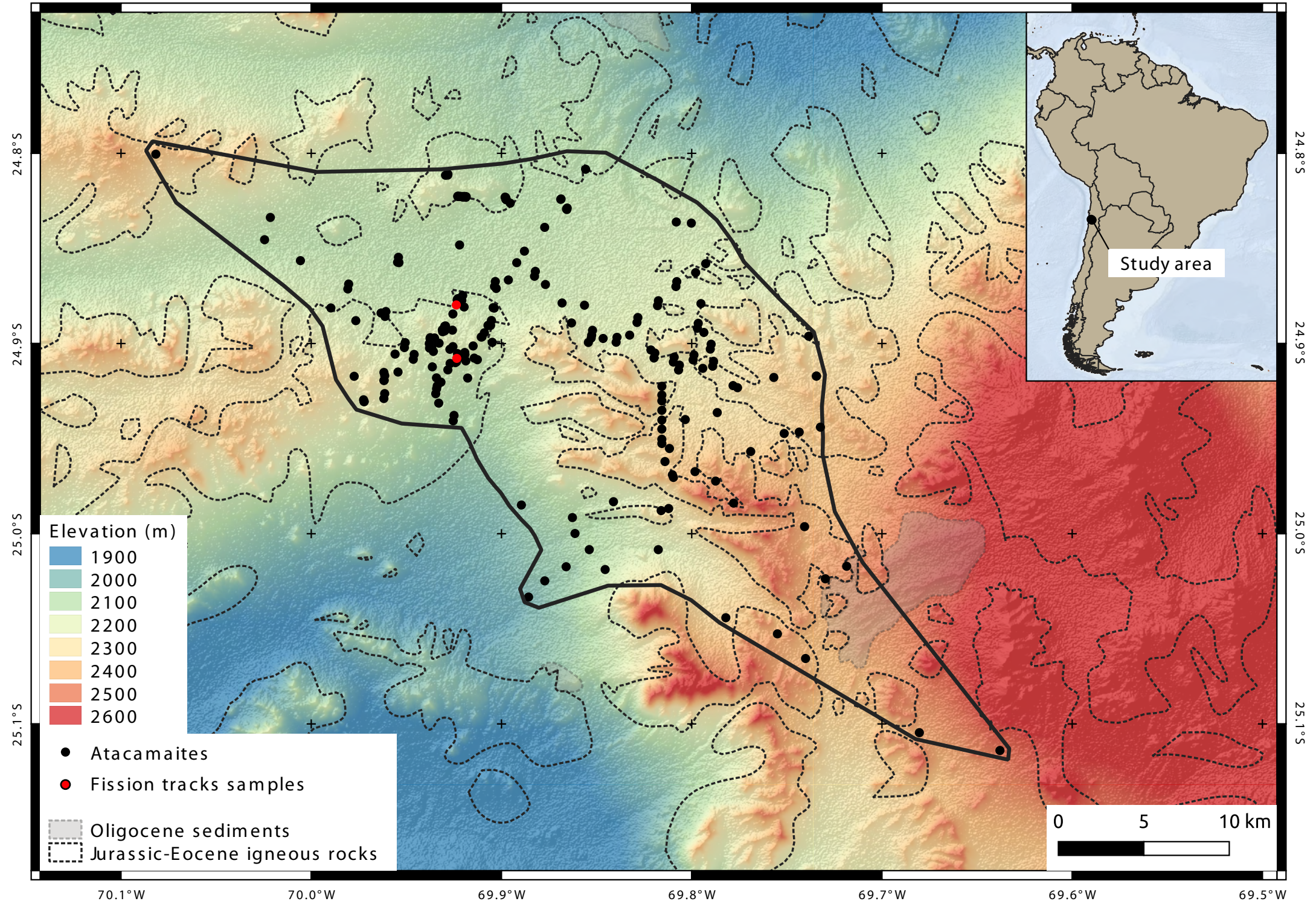












24.8°S

24.9°S

25.0°S

25.1°S

24.8°S

24.9°S

25.0°S

25.1°S

70.1°W

70.0°W

69.9°W

69.8°W

69.7°W

69.6°W

69.5°W

Study area



Click here to access/download  
**Figure (high-resolution)**  
Figure 01 revised.pdf





[Click here to access/download](#)

**Supplementary material for online publication only**  
SOM atacamaite EPSL paper.docx

